

Multifunctional Nanocomposites with High Strength and Capacitance Using 2D MXene and 1D Nanocellulose

Wei-qian Tian, Armin Vahid Mohammadi, Michael S. Reid, Zhen Wang, Liangqi Ouyang,* Johan Erlandsson, Torbjörn Pettersson, Lars Wågberg, Majid Beidaghi, and Mahiar M. Hamedy*

The family of two-dimensional (2D) metal carbides and nitrides, known as MXenes, are among the most promising electrode materials for supercapacitors thanks to their high metal-like electrical conductivity and surface-functional-group-enabled pseudocapacitance. A major drawback of these materials is, however, the low mechanical strength, which prevents their applications in lightweight, flexible electronics. A strategy of assembling freestanding and mechanically robust MXene ($\text{Ti}_3\text{C}_2\text{T}_x$) nanocomposites with one-dimensional (1D) cellulose nanofibrils (CNFs) from their stable colloidal dispersions is reported. The high aspect ratio of CNF (width of ≈ 3.5 nm and length reaching tens of micrometers) and their special interactions with MXene enable nanocomposites with high mechanical strength without sacrificing electrochemical performance. CNF loading up to 20%, for example, shows a remarkably high mechanical strength of 341 MPa (an order of magnitude higher than pristine MXene films of 29 MPa) while still maintaining a high capacitance of 298 F g^{-1} and a high conductivity of 295 S cm^{-1} . It is also demonstrated that MXene/CNF hybrid dispersions can be used as inks to print flexible micro-supercapacitors with precise dimensions. This work paves the way for fabrication of robust multifunctional MXene nanocomposites for printed and lightweight structural devices.

electronics.^[1–3] These materials should be able to withstand extreme mechanical stress and deformations while maintaining high charge storage properties, and thereby decrease the electrochemically inactive weight and volume for packaging of devices, especially in limited spaces.^[1] Most conventional electrode materials, however, fail to meet both requirements.^[4] Some of reported strategies involved using carbon fiber-reinforced composites^[5,6] or graphene-based materials^[1] as structural electrodes to deliver mechanical strength. These materials, however, fall short on the electrochemical energy storage capacitance. Alternatively, metal oxides^[7] or conducting polymers^[8] can be incorporated to boost the capacitance of the graphene-based materials. The problem is the weak interactions between different components, which results in low mechanical stability of the final composites.^[7,9] Therefore, there is a crucial need for the development of new-generation structural energy storage nanocomposites, which monolithically integrate excellent mechanical

Structural electrode materials that integrate high mechanical strength and high electrochemical performances are attractive as they are indispensable for building lightweight, flexible

properties, high electronic and ionic conductivities, and high charge storage capabilities. A balance should also exist between these properties without substantially sacrificing one property over the other.^[1]

Dr. W. Tian, Dr. M. S. Reid, Dr. Z. Wang, Dr. L. Ouyang, J. Erlandsson, Prof. T. Pettersson, Prof. L. Wågberg, Prof. M. M. Hamedy
Department of Fibre and Polymer Technology
KTH Royal Institute of Technology
Teknikringen 56, 10044 Stockholm, Sweden
E-mail: liangqi@kth.se; mahiar@kth.se

Dr. W. Tian, Prof. L. Wågberg, Prof. M. M. Hamedy
Wallenberg Wood Science Centre
Department of Fibre and Polymer Technology
KTH Royal Institute of Technology
Teknikringen 56, 10044 Stockholm, Sweden

Dr. A. Vahid Mohammadi, Prof. M. Beidaghi
Department of Mechanical and Materials Engineering
Auburn University
Auburn, AL 36849, USA

 The ORCID identification number(s) for the author(s) of this article can be found under <https://doi.org/10.1002/adma.201902977>.

The family of two-dimensional (2D) metal carbides and nitrides, collectively known as MXene, are interesting materials for building high-performance supercapacitors.^[10–16] MXenes have a general formula of $\text{M}_{n+1}\text{X}_n\text{T}_x$, where M is an early transition metal such as Ti, X is carbon or nitrogen, and T_x indicates the presence of different functional groups ($-\text{O}$, $-\text{OH}$, and $-\text{F}$) on the surface of metal layers, a result of aqueous exfoliation synthesis of MXenes.^[10,17,18] $\text{Ti}_3\text{C}_2\text{T}_x$ MXene has been widely reported as a high-performance electrode material either in its pristine form or in hybrids with other guest materials such as poly(vinyl alcohol) (PVA),^[18] polypyrrole,^[19,20] and polyaniline,^[21] as well as in hybridization with other carbon materials such as graphene,^[22] carbon nanotubes,^[23–25] and carbon nanofibers.^[26] Most of the MXene hybrid nanocomposites, however, have only shown improvement in either capacitance or mechanical properties while sacrificing one property over the other, and they lack the required mechanical integrity

DOI: 10.1002/adma.201902977

and properties to be considered for practical structural materials for flexible electronics.

We here use carboxymethylated cellulose nanofibrils (CNFs) as a functional additive to assemble with MXenes. CNFs as freestanding films have shown a high toughness and a large strain (larger than 6%) at break.^[27] CNFs also show interesting abilities to disperse and stabilize low-dimension electronic materials such as carbon nanotubes (CNTs),^[28,29] PEDOT,^[30] and graphene,^[31] and can be used as the scaffold/binders for the fabrication of bulky composites.^[30,32–35] The thin dimension of CNFs we used, with a width of ≈ 3.5 nm and length reaching several micrometers, offer the possibility of scaffolding/binding individual MXene flakes into high-strength materials without introducing a high amount of insulating phases between the conductive layers. We show that CNFs and MXene $\text{Ti}_3\text{C}_2\text{T}_x$ colloidal dispersions indeed form stable, homogeneous hybrid at different weight ratios. The freestanding hybrid film made from this hybrid dispersion can simultaneously integrate a high electric conductivity (690 S cm^{-1}), high mechanical strength (154 MPa), high Young's modulus (41.9 GPa), and high specific capacitance (325 F g^{-1}) with 10% CNF loading. To the best of our knowledge, the combination of these values is among the highest reported to date for structural supercapacitor electrodes. These properties stem from the strong interfacial interactions between $\text{Ti}_3\text{C}_2\text{T}_x$ flakes and CNF. We further demonstrate the feasibility of using $\text{Ti}_3\text{C}_2\text{T}_x$ /CNF hybrid for patterning highly flexible functional electronics with the minimum resolution ($\approx 120 \mu\text{m}$) of the gaps between interdigital electrodes.

We prepared the MXene/CNF hybrid dispersions by mixing the colloidal dispersion of delaminated $\text{Ti}_3\text{C}_2\text{T}_x$ ($d\text{-Ti}_3\text{C}_2\text{T}_x$) MXene flakes and carboxymethylated CNFs at different mass ratios (Figure 1a). These two materials are both negatively charged when dispersed in water: the as-prepared $d\text{-Ti}_3\text{C}_2\text{T}_x$ MXene had a zeta potential of -51.4 mV at a pH of 7, and CNF had a zeta potential of -71.8 mV at a pH of 7 (Figure 1b). The individual $\text{Ti}_3\text{C}_2\text{T}_x$ flakes are around 2 nm thick and several hundred nm in lateral size (Figure 1c,d). We prepared carboxymethylated CNFs from a fully bleached sulfite pulp from Scandinavian softwood that was subsequently carboxymethylated to a charge around $600 \mu\text{mol g}^{-1}$.^[36] The individual nanofibrils have a high aspect ratio with a uniformly square cross-section of around 3.5 nm and length up to several micrometers (Figure 1e,f). Figure 1b shows the zeta potential change of $\text{Ti}_3\text{C}_2\text{T}_x$ /CNF hybrid dispersions with the different mass concentration of CNF as a function of the time. The hybrid dispersions showed high stability with insignificant changes in the zeta potential, such as $\text{Ti}_3\text{C}_2\text{T}_x$ -20% CNF with a zeta potential of -52.9 mV after one month. Over this period, the hybrid dispersions did not have any precipitates or phase separations, suggesting a stable blend of the two colloids.

To study the interaction between the two phases, we used colloidal probe atomic force microscopy (AFM)^[29] in liquid to measure the interfacial interaction between MXene flakes and nanocellulose fibrils. We selected a model system consisting of a planar surface coated with $\text{Ti}_3\text{C}_2\text{T}_x$ flakes and a probe coated with CNFs (for details see the Experimental Section and Figure S1a of the Supporting Information). Figure 1g,h shows the force–distance measurements between $\text{Ti}_3\text{C}_2\text{T}_x$ flake's surface and the CNF-coated probe upon approach and

on separation in liquid (Milli-Q water and NaCl solution). The approach data (Figure 1g; Figure S1b, Supporting Information) show long-range electrostatic repulsion for all solutions containing NaCl (10^{-6} to 10^{-3} M) whereas for pure water there is also an attractive force at separations less than $\approx 50 \text{ nm}$. We propose that electrostatic forces between CNFs and $\text{Ti}_3\text{C}_2\text{T}_x$ flakes are responsible for the long-range repulsion, which in turn favor the stabilization of the dispersion. The separation data (Figure 1h) show the force required to separate the two surfaces. We calculated the adhesion between $\text{Ti}_3\text{C}_2\text{T}_x$ surface and the CNF-coated probe as shown in Figure 1i. The adhesion decreased from 1.0 mJ m^{-2} in Milli-Q water to 0.4 mJ m^{-2} in 10^{-5} M NaCl. This result is consistent with our previous reports for graphene–CNF system.^[29] We attribute the adhesion between the $\text{Ti}_3\text{C}_2\text{T}_x$ flakes and CNFs to the functional groups ($-\text{OH}$, $-\text{O}$, $-\text{F}$) present on the outer transition metal layer surface of $\text{Ti}_3\text{C}_2\text{T}_x$ flakes. Additionally, these results indicate that the highest adhesion between the surfaces can be achieved at the low ionic strength regime, i.e., Milli-Q water. We, therefore, conducted all fabrication of $\text{Ti}_3\text{C}_2\text{T}_x$ /CNF composites in water.

The attraction force between CNFs and $\text{Ti}_3\text{C}_2\text{T}_x$ flakes offers an excellent opportunity of binding MXene flakes with a strong CNF scaffold. We fabricated freestanding composite nanopapers made from $\text{Ti}_3\text{C}_2\text{T}_x$ /CNF dispersions using vacuum filtration (Figure 2a). Figure 2, and Figures S2 and S3 (Supporting Information) show the morphologies of the freestanding nanopapers of pristine $\text{Ti}_3\text{C}_2\text{T}_x$ MXene and CNF as well as their composites. We found that the composites have similar layered structures as the pristine MXene films. With the increase of CNF loading, nanofibril structures appeared at the cross-sectional view of layers and even between adjacent layers. We note that the freestanding nanopapers possess smooth surfaces even at high CNF loading, with a roughness R_a of around 10 nm from a $3 \times 3 \mu\text{m}^2$ area (Figure S3, Supporting Information).

XRD pattern (Figure 3a) of the pristine $\text{Ti}_3\text{C}_2\text{T}_x$ MXene shows clear diffraction peaks related to MXene basal planes. The peak at 6.9° (d -spacing of 12.8 \AA) corresponds to (0002) planes of MXenes. This peak moved from 6.1° to 5.3° as CNF loading increased from 5% to 40%, corresponding to a shift in the (0002) planes' distance from 14.4 to 16.7 \AA . These results suggest a substantial amount of CNF incorporated into nanocomposites as a function of CNF content, which is in agreement with the data of FTIR and contact angles (Figure S4, Supporting Information).

Loading of CNF to the MXene films significantly enhanced the mechanical strength of the MXene $\text{Ti}_3\text{C}_2\text{T}_x$ /CNF nanocomposites. The freestanding films of $\text{Ti}_3\text{C}_2\text{T}_x$ /CNF can be folded or wrapped into various shapes without any cracking (Figure 2b). The tensile strength, i.e., stress at break, of $\text{Ti}_3\text{C}_2\text{T}_x$ -5% CNF increased significantly to 68.0 from 25.8 MPa for pristine MXene $\text{Ti}_3\text{C}_2\text{T}_x$ film (Figure 3d, Figure S5 (Supporting Information), and Table 1). The tensile strength increased up to 271.5 MPa for $\text{Ti}_3\text{C}_2\text{T}_x$ -60% CNF, which is around an order of magnitude higher than pristine MXene films, and is more than two-times higher than that of previously reported $\text{Ti}_3\text{C}_2\text{T}_x$ /CNF composites (with the highest tensile strength of 135 MPa).^[37]

To demonstrate the effect of the geometry of nanocellulose on the composite, we also used cellulose nanocrystals (CNCs) which are shorter than CNF to build MXene/CNF composites.

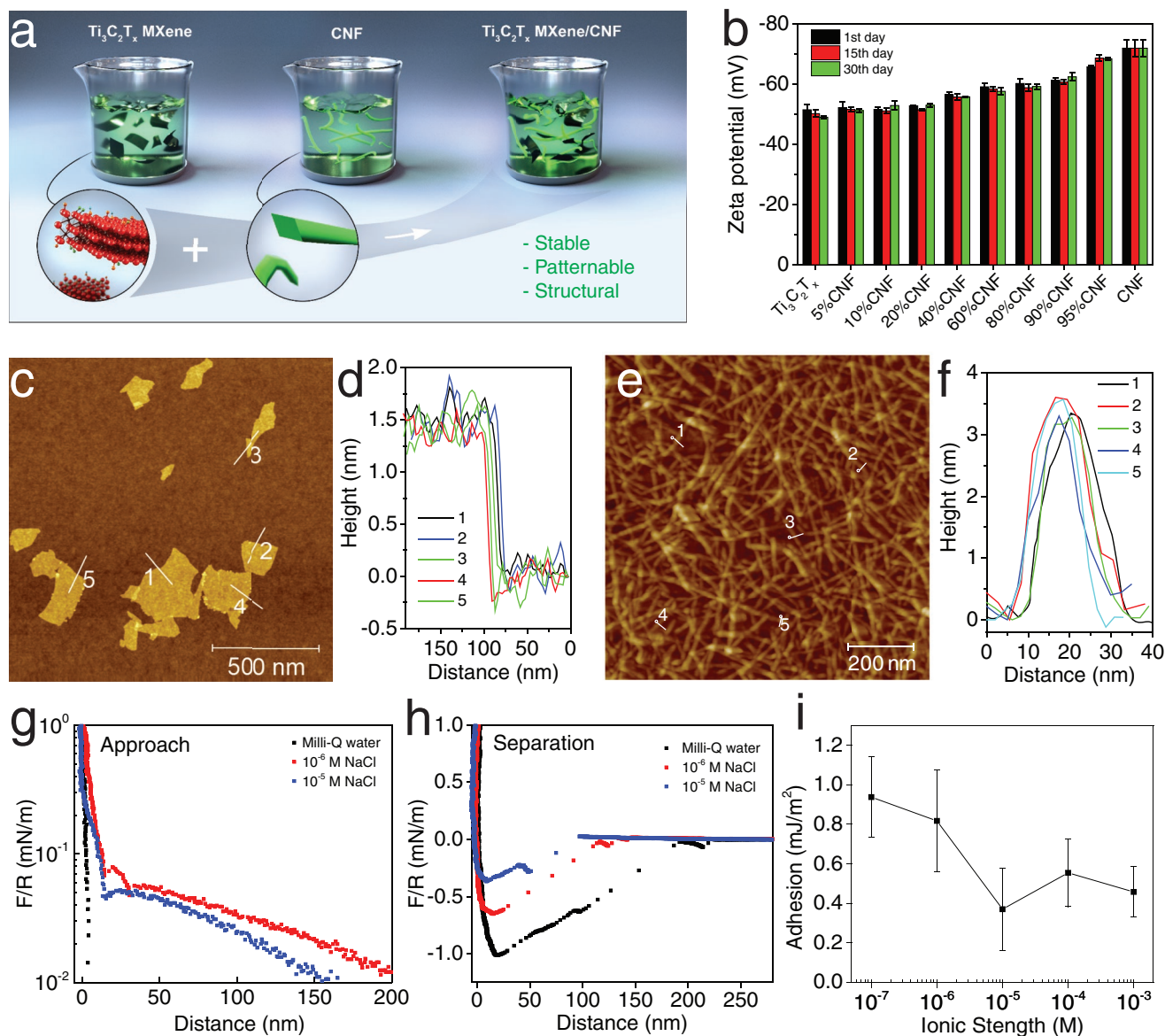


Figure 1. $\text{Ti}_3\text{C}_2\text{T}_x$ MXene/CNF hybrid. a) Schematics of $\text{Ti}_3\text{C}_2\text{T}_x$ /CNF hybrid dispersion. b) Zeta potentials of $\text{Ti}_3\text{C}_2\text{T}_x$ /CNF dispersions at different times as a function of CNF contents. c–f) AFM height image and the corresponding height profile along the crossed lines for $\text{Ti}_3\text{C}_2\text{T}_x$ MXene (c,d) and CNF dispersion (e,f). g,h) Force/radius (F/R) versus distance curves between the interfaces of $\text{Ti}_3\text{C}_2\text{T}_x$ flakes and cantilever coated with CNF upon approach (g) and separation (h) in liquid. i) Adhesion as a function of the ionic strength between the interfaces of $\text{Ti}_3\text{C}_2\text{T}_x$ flakes and CNF.

As shown in Figure S6 of the Supporting Information, CNFs are slightly wider than CNF with a width of ≈ 10 nm. Yet these nanocrystals are several orders of magnitude shorter than the nanofibrils. We found that CNFs also enable to form nanocomposite with MXene $\text{Ti}_3\text{C}_2\text{T}_x$ (Figure S7, Supporting Information), but the $\text{Ti}_3\text{C}_2\text{T}_x$ /CNF nanocomposite films became brittle and shattered into pieces when CNC loading exceeded 20% (Figure S9, Supporting Information). XRD data of $\text{Ti}_3\text{C}_2\text{T}_x$ /CNF show, almost, an unchanged position of (0002) peak and rapidly decreasing diffraction intensity with increasing CNC loading compared to that of the pristine MXene film (Figure 3b), suggesting that the CNC does not effectively incorporate into between adjacent MXene layers. This is consistent with the

observation from AFM data of $\text{Ti}_3\text{C}_2\text{T}_x$ /CNC films that show a lot of CNC clusters on the surface of films (Figure S10, Supporting Information). As expected, the $\text{Ti}_3\text{C}_2\text{T}_x$ /CNC nanocomposites showed no significant enhancement in the mechanical properties, probably due to a combination of the short length of CNC with an aspect ratio of 10–30 and its inability to effectively entangle MXene flakes (Figure S11, Supporting Information).

These results suggest that the improvement in MXene/CNF mechanical strength originates from two factors. (1) Strong interfacial interactions, originating mostly from van der Waals interactions between the materials with possible contributions from hydrogen bonding between the hydroxyl and carboxylic terminations of CNFs and the hydroxyl termination groups of

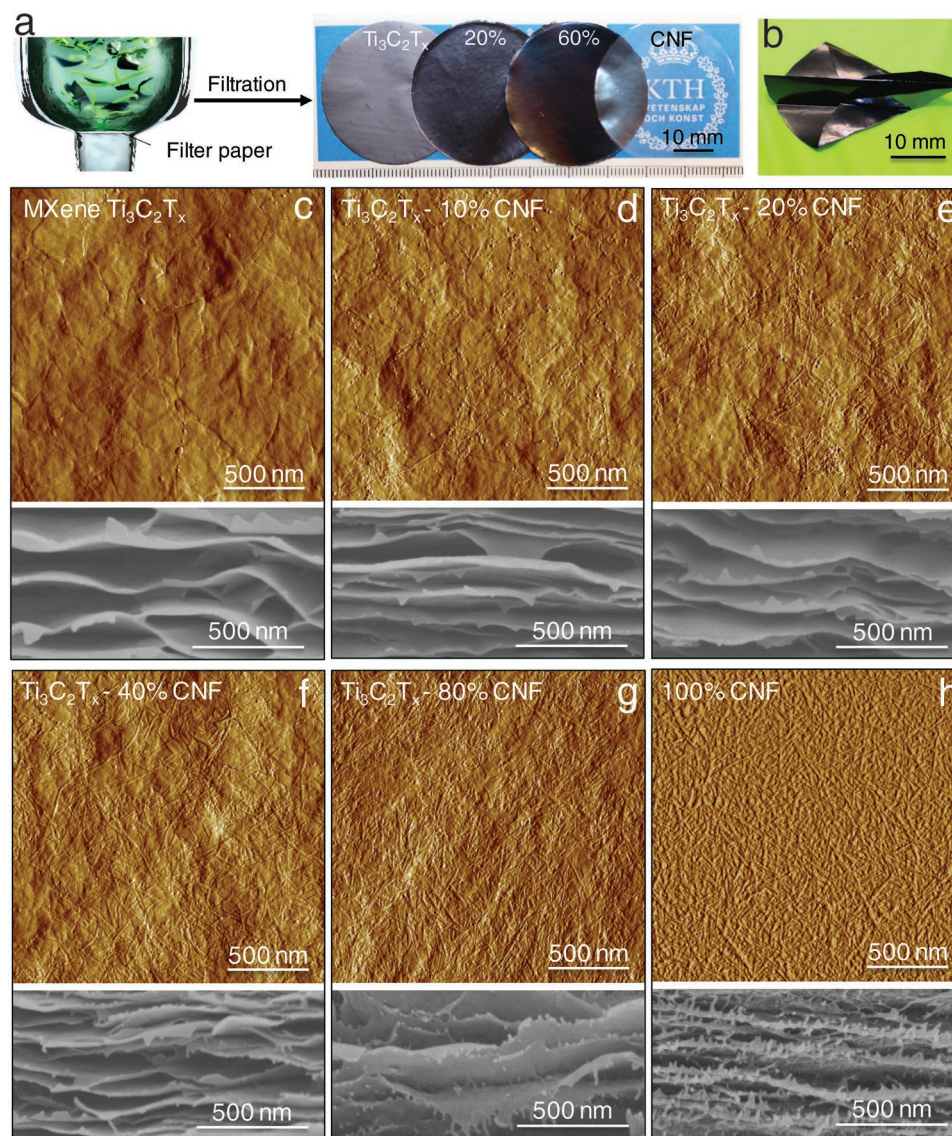


Figure 2. Morphology characterization of $\text{Ti}_3\text{C}_2\text{T}_x$ MXene/CNF nanopapers. a) Schematics for the fabrication of $\text{Ti}_3\text{C}_2\text{T}_x$ /CNF nanopapers and their digital photographs. b) Photography of a $\text{Ti}_3\text{C}_2\text{T}_x$ /CNF nanopaper folded into a shape of airplane to show the mechanical flexibility. c–h) AFM peak-force error images (top) and SEM cross-sectional images (bottom) of $\text{Ti}_3\text{C}_2\text{T}_x$ MXene (c), $\text{Ti}_3\text{C}_2\text{T}_x$ -10% CNF (d), $\text{Ti}_3\text{C}_2\text{T}_x$ -20% CNF (e), $\text{Ti}_3\text{C}_2\text{T}_x$ -40% CNF (f), $\text{Ti}_3\text{C}_2\text{T}_x$ -80% CNF (g), and pristine CNF papers (h). For AFM images the corresponding height images are presented in Figure S3 of the Supporting Information.

MXene flake.^[18,37] (2) The geometrical proportions between the 1D and 2D materials, where the CNF, which is thin, yet longer than the MXene flakes, serve as bridges to bind MXenes on the same plane and locks the adjacent layers. This bridging does not occur for shorter CNCs (Figure S11, Supporting Information).

We were able to further improve the mechanical strength of the fabricated $\text{Ti}_3\text{C}_2\text{T}_x$ /CNF nanopapers by using a vacuum pressing process. After vacuum pressing, the nanopapers with 5% CNF, 10% CNF, 20% CNF, 40% CNF, and 60% CNF showed an enhanced tensile strength of 139.1, 181.3, 340.6, 416.1, 339.4, and 330.1 MPa, respectively (Figure 3c,d). These values are higher than the initial tensile strength of the $\text{Ti}_3\text{C}_2\text{T}_x$ /CNF (Figure S5 and Table S1, Supporting Information) because

vacuum-pressed nanopapers form stronger percolating CNF networks, and a more compact structure with stronger interactions between CNF and MXene. The XRD data of $\text{Ti}_3\text{C}_2\text{T}_x$ /CNF (Figure S12, Supporting Information) shows a decrease in the d -spacing after vacuum-pressing, because some intercalated water between $\text{Ti}_3\text{C}_2\text{T}_x$ /CNF dries out of the structure. We hypothesize that the use of other CNFs with more functional groups, such as TEMPO (2,2,6,6-tetramethyl 1-piperidinyloxy) modified CNF, could further enhance the structural properties of the $\text{Ti}_3\text{C}_2\text{T}_x$ /CNF nanocomposites.^[38]

The electrical conductivity of the $\text{Ti}_3\text{C}_2\text{T}_x$ /CNF films can also be tailored by varying the CNF content. Pristine $\text{Ti}_3\text{C}_2\text{T}_x$ films fabricated using vacuum filtration had a conductivity of $1.85 \times 10^5 \text{ S m}^{-1}$, Figure 3e. 5% CNF loading slightly decreased

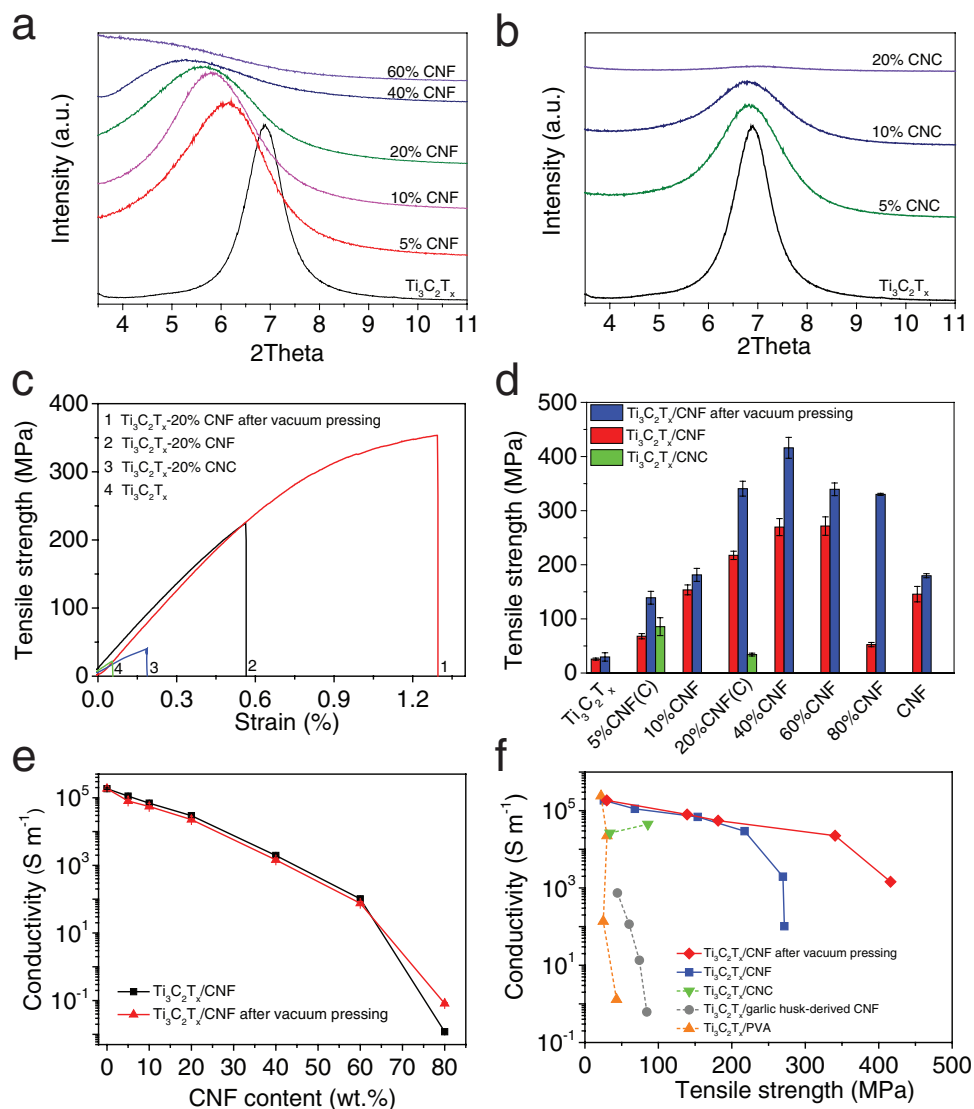


Figure 3. Physical properties of $\text{Ti}_3\text{C}_2\text{T}_x$ MXene/nanocellulose nanopapers. a) XRD patterns of $\text{Ti}_3\text{C}_2\text{T}_x/\text{CNF}$ nanopapers with bound water as a function of CNF contents. b) XRD patterns of $\text{Ti}_3\text{C}_2\text{T}_x/\text{CNC}$ nanocomposites with bound water as a function of CNC contents. c) Tensile stress–strain curves of $\text{Ti}_3\text{C}_2\text{T}_x$ -20% CNF before and after vacuum pressing, $\text{Ti}_3\text{C}_2\text{T}_x$ -20% CNC, and $\text{Ti}_3\text{C}_2\text{T}_x$ papers. d) Tensile strength of $\text{Ti}_3\text{C}_2\text{T}_x/\text{CNF}$ (or CNC) nanopapers before and after vacuum pressing. e) Electronic conductivity of $\text{Ti}_3\text{C}_2\text{T}_x/\text{CNF}$ nanopapers before and after vacuum pressing versus CNF contents. f) Ashby plot of tensile strength versus conductivity for $\text{Ti}_3\text{C}_2\text{T}_x/\text{CNF}$ nanopapers compared with other $\text{Ti}_3\text{C}_2\text{T}_x$ -based composites.

the conductivity to $1.12 \times 10^5 \text{ S m}^{-1}$, and after increasing the CNF loading to 20%, a high conductivity of $2.95 \times 10^4 \text{ S m}^{-1}$ was still retained (Table 1). As shown in Figure S13 of the Supporting Information, $\text{Ti}_3\text{C}_2\text{T}_x/\text{CNF}$ nanopapers have higher electronic conductivity than those reported for $\text{Ti}_3\text{C}_2\text{T}_x/\text{PVA}$ composites at similar loading ratios of the organic materials.^[17] The conductivity values of $\text{Ti}_3\text{C}_2\text{T}_x/\text{CNF}$ nanopapers are even several order of magnitude higher than previously reported $\text{Ti}_3\text{C}_2\text{T}_x/\text{garlic husk-derived CNF}$ composites (that used CNFs with width of 20–50 nm).^[37] We hypothesize that the higher conductivity is attributed to the thinner CNF dimension ($\approx 3.5 \text{ nm}$), which may reduce the insulating gaps between $\text{Ti}_3\text{C}_2\text{T}_x$ flakes. Ashby plot (Figure 3f) of conductivities versus tensile strengths, highlights that our $\text{Ti}_3\text{C}_2\text{T}_x/\text{CNF}$ nanopapers have better integration of mechanical properties and electronic

conductivities, than other reported MXene-based structural composites. This improvement is required for high-performance structural energy storage.

To evaluate the electrochemical properties of the $\text{Ti}_3\text{C}_2\text{T}_x/\text{CNF}$ nanocomposite and understand the effect of CNF contents on their charge storage properties, we conducted electrochemical measurements in a three-electrode setup using 3 M sulfuric acid as the electrolyte. Figure 4a schematically shows the three-electrode setup used in our experiment. Cyclic voltammogram (CV) curves of $\text{Ti}_3\text{C}_2\text{T}_x$ MXene and different $\text{Ti}_3\text{C}_2\text{T}_x/\text{CNF}$ nanopaper electrodes are shown in Figure 4b and Figure S14 (Supporting Information). The addition of CNF to $\text{Ti}_3\text{C}_2\text{T}_x$ MXene does not significantly lower the capacitance of the nanocomposites compared to the pristine MXene paper, and the vacuum pressing has negligible effect on the response and capacitances

Table 1. Physical properties of $\text{Ti}_3\text{C}_2\text{T}_x$ MXene, $\text{Ti}_3\text{C}_2\text{T}_x/\text{CNF}$, and CNF papers.

Samples	2θ [°]	d -spacing [Å]	Conductivity [S m^{-1}]	Contact angle [°]	Mechanical properties		
					Tensile strength [MPa]	Strain at fracture [%]	Young's modulus [GPa]
MXene $\text{Ti}_3\text{C}_2\text{T}_x$	6.90	12.80	1.85×10^5	68	25.8 ± 1.9	0.10 ± 0.08	22.3 ± 5.9
$\text{Ti}_3\text{C}_2\text{T}_x$ -5% CNF	6.14	14.38	1.12×10^5	63	68.0 ± 4.8	0.16 ± 0.11	41.4 ± 0.2
$\text{Ti}_3\text{C}_2\text{T}_x$ -10% CNF	5.99	14.74	6.90×10^4	57	153.6 ± 9.1	0.39 ± 0.04	41.9 ± 2.6
$\text{Ti}_3\text{C}_2\text{T}_x$ -20% CNF	5.80	15.23	2.95×10^4	48	217.4 ± 7.7	0.57 ± 0.03	41.0 ± 1.8
$\text{Ti}_3\text{C}_2\text{T}_x$ -40% CNF	5.28	16.73	1.96×10^3	35	269.6 ± 15.7	1.92 ± 0.38	26.6 ± 2.5
$\text{Ti}_3\text{C}_2\text{T}_x$ -60% CNF	–	–	1.02×10^2	30	271.5 ± 17.7	2.18 ± 0.11	18.5 ± 1.8
$\text{Ti}_3\text{C}_2\text{T}_x$ -80% CNF	–	–	1.17×10^{-2}	24	52.5 ± 3.9	1.32 ± 0.83	6.58 ± 2.7
$\text{Ti}_3\text{C}_2\text{T}_x$ -5% CNC	6.84	12.91	4.46×10^4	62	85.7 ± 16.4	0.87 ± 0.24	16.8 ± 1.9
$\text{Ti}_3\text{C}_2\text{T}_x$ -20% CNC	–	–	2.63×10^4	32	34.1 ± 2.6	0.17 ± 0.09	20.2 ± 2.9
CNF	–	–	–	22	145.7 ± 14.3	3.15 ± 0.33	8.25 ± 0.4

of the $\text{Ti}_3\text{C}_2\text{T}_x/\text{CNF}$ nanopaper electrodes (Figure S15, Supporting Information). When the CNF loading is below 20 wt%, the composite electrodes showed mostly capacitive behavior with signature redox peaks associated with the protonation and change in the oxidation status of Ti atoms^[39,40] as shown in Figure 4c for $\text{Ti}_3\text{C}_2\text{T}_x$ -5% CNF electrode (and Figure S14 of the Supporting Information for other compositions). We measured gravimetric capacitances of 369, 324, and 298 F g^{-1} for $\text{Ti}_3\text{C}_2\text{T}_x/\text{CNF}$ nanocomposite electrodes with 5%, 10%, and 20% CNF loadings, respectively, at a scan rate of 2 mV s^{-1} (Figure 4d). The capacitance decreased with CNF loading because CNF is electrochemically inactive in the potential window of $\text{Ti}_3\text{C}_2\text{T}_x$.^[18] Figure 4d,e, shows the normalized capacitances of different $\text{Ti}_3\text{C}_2\text{T}_x/\text{CNF}$ nanocomposites. Figure S16 of the Supporting Information shows the gravimetric capacitances of $\text{Ti}_3\text{C}_2\text{T}_x/\text{CNF}$ nanocomposites with a linear decrease by increasing CNF loading from 5 to 20 wt%. For example, the capacitances of the $\text{Ti}_3\text{C}_2\text{T}_x$ -5% CNF ($\approx 332 \text{ F g}^{-1}$) or $\text{Ti}_3\text{C}_2\text{T}_x$ -20% CNF (285 F g^{-1}) is only $\approx 5\%$ or $\approx 20\%$ less than that of the pristine $\text{Ti}_3\text{C}_2\text{T}_x$ film (348 F g^{-1}) at a scan rate of 5 mV s^{-1} . The inset of Figure 4d shows that the normalized gravimetric capacitances, calculated solely based on the weight of $\text{Ti}_3\text{C}_2\text{T}_x$ using the composition ratios of the initial hybrid dispersions, remain almost the same for all electrodes, demonstrating the identical amount of $\text{Ti}_3\text{C}_2\text{T}_x$ used in the preparation of the films. This suggests that the composition of the $\text{Ti}_3\text{C}_2\text{T}_x/\text{CNF}$ nanocomposite films is close to the composition of the initial hybrid dispersions. This happens because the length of CNF and the lateral size of MXene particles are both larger than the pore size of PVDF membrane, and because the extremely large aspect ratio of CNFs (>300) promotes entanglement of the fibers,^[30] which create a scaffold structure to support the MXene flakes.

The addition of only 5% CNF to $\text{Ti}_3\text{C}_2\text{T}_x$ resulted in a negligible decrease (around 5%) in the gravimetric capacitance of the nanocomposite electrode with a very similar rate-capability to that of pristine MXene paper electrode. The mechanical strength of the $\text{Ti}_3\text{C}_2\text{T}_x$ -5% CNF electrode, however, increased by 260% from 25.8 to 68.0 MPa. The increase in mechanical strength is more significant for $\text{Ti}_3\text{C}_2\text{T}_x$ -20% CNF nanocomposite paper which showed an order of magnitude higher mechanical strength ($\approx 217 \text{ MPa}$) with only 20%

lower gravimetric capacitance. The significant improvement in the mechanical strength of the fabricated paper electrodes thus overweighs the slight decrease in their electrochemical properties and renders them especially useful in applications where structural multifunctional electrodes with high mechanical robustness as well as high capacitances are required. The semilog plot of the gravimetric capacitance versus mechanical strength in Figure 4f, shows that the $\text{Ti}_3\text{C}_2\text{T}_x/\text{CNF}$ nanopaper electrodes display the best integration of the capacitance and mechanical strength among some of the previously reported notable multifunctional supercapacitor electrodes such as MXene/rGO,^[41] MXene/PVA,^[18] rGO/Aramid nanofiber,^[1] rGO/cellulose,^[9] rGO and rGO/PANI,^[8] rGO/ MnO_2 ,^[7] and CNT/PPy.^[42] This indicates that in $\text{Ti}_3\text{C}_2\text{T}_x/\text{CNF}$ composites, an optimized trade-off between mechanical properties and energy storage is obtained, where the mechanical strength is significantly improved compared to pristine $\text{Ti}_3\text{C}_2\text{T}_x$ while the electrochemical properties of $\text{Ti}_3\text{C}_2\text{T}_x$ MXene are mostly retained.

Figure 4g shows the electrochemical impedance spectroscopy results for $\text{Ti}_3\text{C}_2\text{T}_x/\text{CNF}$ electrodes. As shown, addition of CNF resulted in a small increase in the ion transport resistance of the hybrid electrodes as evident from the Nyquist plots and in a good agreement with CV experiments. The electrodes, however, showed almost a vertical rise in the imaginary impedance at low frequencies indicating the facile accessibility of electrolyte's ions to charge storage sites on the surface of titanium carbide layers. CNFs act as spacers in between MXene layers and improve the proton transport in the nanocomposite electrode.^[25,43,44] We compared the capacitive response of the nanocomposite electrodes to that of pristine MXene electrodes by considering a power-law relationship between the peak current (i_p) and scan rate (ν), ($i_p = a\nu^b$).^[45,46] In this equation "a" and "b" are variables, where $b = 0.5$ corresponds to diffusion-limited reactions and $b \approx 1$ corresponds to surface-controlled (capacitive) reactions. All $\text{Ti}_3\text{C}_2\text{T}_x/\text{CNF}$ nanopaper electrodes displayed a similar capacitive response to that of the pristine MXene film (Figure 4h), with a highly capacitive charge storage properties up to scan rates of 200 mV s^{-1} . These results further show that the addition of CNF does not significantly impact the rate-capability and capacitive charge storage mechanism in $\text{Ti}_3\text{C}_2\text{T}_x/\text{CNF}$ nanocomposite electrodes but does significantly

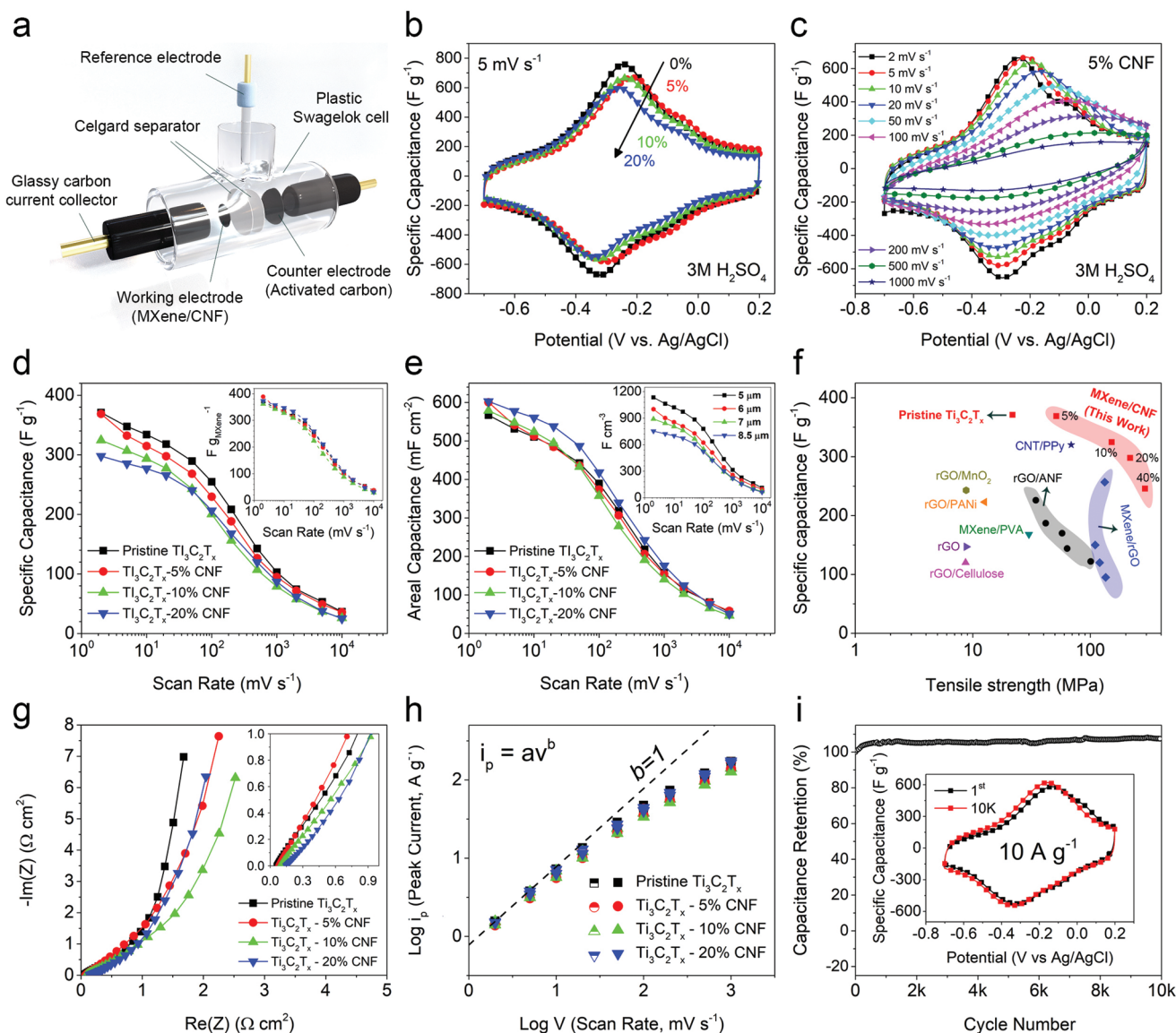


Figure 4. Electrochemical performances of Ti₃C₂T_x MXene/CNF paper electrodes. a) Schematic illustration of the three-electrode setup used in this work. b) Comparison between cyclic voltammograms (CVs) of pristine Ti₃C₂T_x MXene, Ti₃C₂T_x-5% CNF, Ti₃C₂T_x-10% CNF, and Ti₃C₂T_x-20% CNF paper electrodes. c) CVs of Ti₃C₂T_x-5% CNF paper electrode at scan rates from 2 mV s⁻¹ to 1 V s⁻¹. d) gravimetric capacitance of the electrodes. Inset shows gravimetric capacitance of the electrodes just based on the Ti₃C₂T_x weight, confirming similar amount of MXene used in the preparation of the films and almost similar capacitance values for all of them. e) Areal capacitance and, in the inset, volumetric capacitance of the electrodes. f) Comparison of the capacitance versus mechanical strength of the MXene/Ti₃C₂T_x/CNF paper with some other notable reported multifunctional composites in the literature. g) Electrochemical impedance spectroscopy (EIS) data of the Ti₃C₂T_x/CNF electrodes. The resistance values are normalized over the area of the electrode (cm²). h) Logarithmic of the anodic and cathodic peak currents at different scan rates for Ti₃C₂T_x/CNF paper electrodes. i) Cycle life of the Ti₃C₂T_x-5% CNF paper electrode at 10 A g⁻¹. The inset shows CV profiles of the electrode at the first cycle and after 10K cycles at a scan rate of 20 mV s⁻¹.

increase their mechanical strength. We also investigated the cyclic performance of the Ti₃C₂T_x/CNF nanopaper electrodes in 3 M sulfuric acid electrolyte, as shown in Figure 4i where a Ti₃C₂T_x-5% CNF showed almost a 100% capacitance retention after 10 000 cycles at a charging/discharging rate of 10 A g⁻¹.

We fabricated micro-supercapacitors by employing a combined process of wax printing and vacuum-assisted filtration as shown in Figure 5a. The micro-supercapacitor structures (Figure 5b) had a resolution of ≈900 μm width and 1 cm length for interdigitated electrodes, and ≈130 μm gaps between the

individual electrodes (Figure 5c), which is smaller than those previously reported for laser patterning method (450 μm gaps).^[47] Top-view SEM images of micro-supercapacitor exhibit some wrinkles resulting from the porous structure of the filter membrane, while the cross-sectional SEM image of the electrodes show stacked layers similar to Ti₃C₂T_x/CNF nanopapers (Figure 5d,e). We could control the thickness of the printed electrodes to around 1.7 μm for Ti₃C₂T_x-10% CNF electrodes and fabricate interdigitated electrodes with well-defined edges and good separation between the fingers. We

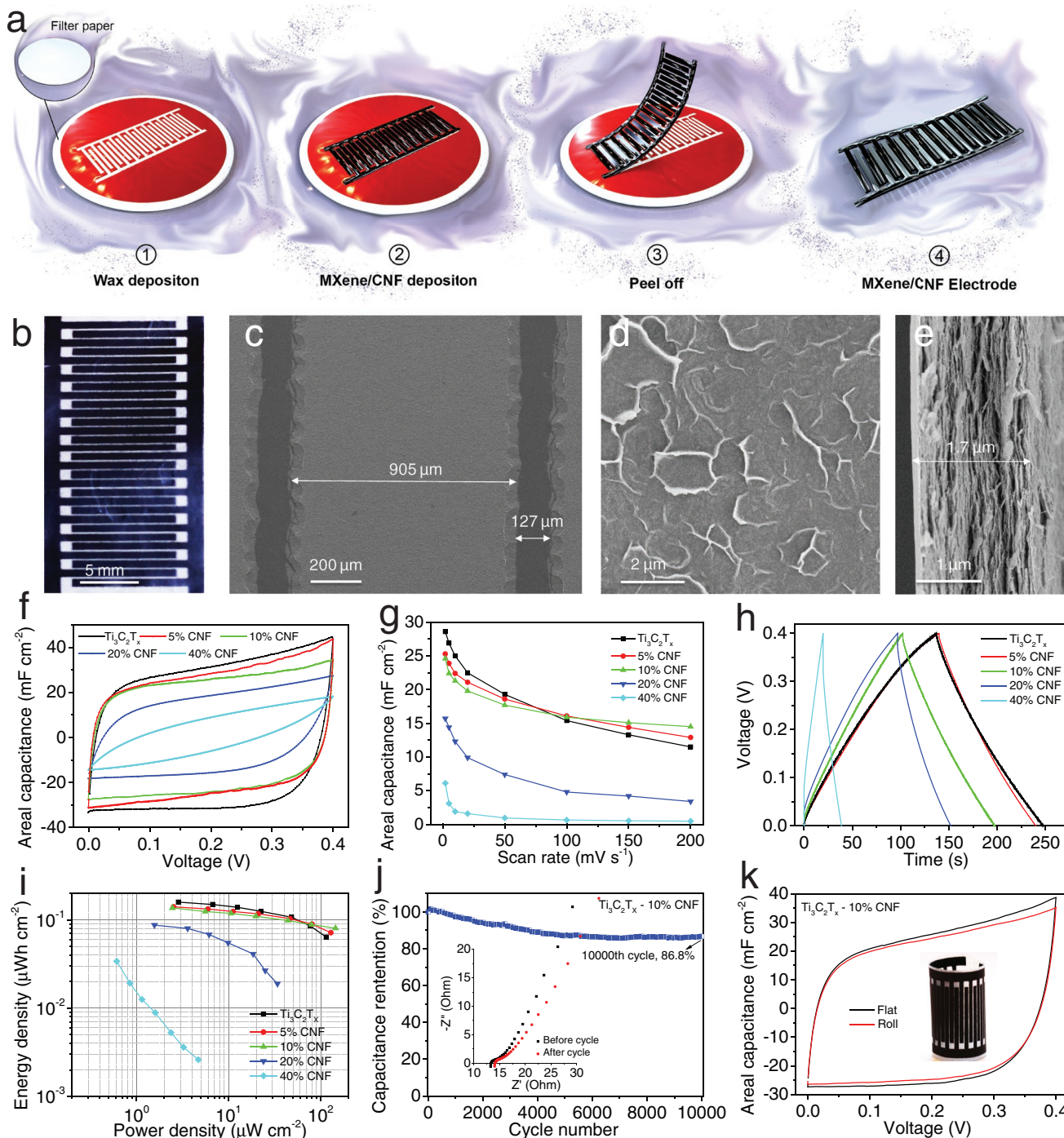


Figure 5. Electrochemical performances of $\text{Ti}_3\text{C}_2\text{T}_x$ MXene/CNF-based micro-supercapacitors. a) Schematic illustration showing different fabrication steps for $\text{Ti}_3\text{C}_2\text{T}_x$ /CNF-based micro-supercapacitors. b) Digital photograph of the micro-supercapacitor with $\text{Ti}_3\text{C}_2\text{T}_x$ /CNF electrodes. c, d) Top-view, and e) cross-sectional SEM images of micro-supercapacitors based on $\text{Ti}_3\text{C}_2\text{T}_x$ -10% CNF electrode. f) CV curves at a scan rate of 2 mV s^{-1} , g) specific capacitances at different scan rates, h) charge/discharge profiles at 0.06 mA cm^{-2} and i) Ragone plot for $\text{Ti}_3\text{C}_2\text{T}_x$ /CNF-based micro-supercapacitors. j) Cyclic stability and k) CV curves at a flat and roll status of $\text{Ti}_3\text{C}_2\text{T}_x$ -10% CNF-based micro-supercapacitors.

transferred the patterned electrodes onto flexible substrates using scotch tape. The successful fabrication of $\text{Ti}_3\text{C}_2\text{T}_x$ /CNF-based micro-supercapacitors through our approach was attributed to the functionality of CNFs, which increase the contact angle and the patternability of the $\text{Ti}_3\text{C}_2\text{T}_x$ /CNF

dispersions and improves the mechanical properties of the $\text{Ti}_3\text{C}_2\text{T}_x$ /CNF electrodes, for flexible printed electronics. Without using any metal current collectors, the $\text{Ti}_3\text{C}_2\text{T}_x$ /CNF electrodes could act as both the current collector and active material in the fabricated micro-supercapacitors to store

electrochemical energy. The symmetric $\text{Ti}_3\text{C}_2\text{T}_x/\text{CNF}$ -based interdigitated micro-supercapacitors displayed ideal capacitive behaviors as shown in Figure 5f,h. The $\text{Ti}_3\text{C}_2\text{T}_x$ -5% CNF-based micro-supercapacitor displayed a specific capacitance of 25.3 mF cm^{-2} at a scan rate of 2 mV s^{-1} , similar to the value of 28.6 mF cm^{-2} (2 mV s^{-1}) for pristine $\text{Ti}_3\text{C}_2\text{T}_x$ MXene-based micro-supercapacitor (Figure 5g). The micro-supercapacitors fabricated with CNF loadings of up to 10 wt% only showed a slightly lower capacitance (Figure 5g), at higher rates while maintaining a comparable performance with that of pristine $\text{Ti}_3\text{C}_2\text{T}_x$ MXene-based micro-supercapacitor. Among the different fabricated micro-supercapacitors, the $\text{Ti}_3\text{C}_2\text{T}_x$ -10% CNF-based device showed the best rate performance (Figure 5f; Figures S17 and S18). In addition, the $\text{Ti}_3\text{C}_2\text{T}_x/\text{CNF}$ -based micro-supercapacitors could deliver a high integrated output of energy and power densities, with an energy density of $0.08 \text{ } \mu\text{Wh cm}^{-2}$ at the power density of $145 \text{ } \mu\text{W cm}^{-2}$ (Figure 5i). The fabricated $\text{Ti}_3\text{C}_2\text{T}_x/\text{CNF}$ micro-supercapacitors also showed excellent life cycle. For example, the $\text{Ti}_3\text{C}_2\text{T}_x$ -10% CNF micro-supercapacitor exhibited a capacitance retention of 86.8% after 10 000 cycles at a current density of 0.57 mA cm^{-2} (Figure 5j). In addition, because of the enhanced mechanical properties of the $\text{Ti}_3\text{C}_2\text{T}_x/\text{CNF}$ electrodes, the fabricated micro-supercapacitor devices could be bent and rolled without noticeable degradation in their charge storage performance as shown in Figure 5k.

The combination of these properties renders the $\text{Ti}_3\text{C}_2\text{T}_x/\text{CNF}$ hybrid and their printed structures as promising electrode materials for flexible energy storage devices and printed electronics. For example, $\text{Ti}_3\text{C}_2\text{T}_x/\text{CNF}$ hybrid can be used to fabricate paper-based microfluidic and electronic structures on a wax-defined paper, with a minimum feature size of $800 \text{ } \mu\text{m}$ for conductive wires (Figures S19–S22, Supporting Information). This is attributed to the strong interaction between $\text{Ti}_3\text{C}_2\text{T}_x$ flakes and cellulose fibers from the hybrid dispersion and also from the paper-based substrates, as we showed in our AFM force measurements earlier.

In summary, we have demonstrated that a blend of aqueous dispersions of the 2D material, $\text{Ti}_3\text{C}_2\text{T}_x$ MXene, and the 1D material, cellulose nanofibrils CNFs can be used to rationally design and fabricate multifunctional nanocomposites with three notable properties. (1) A high mechanical strength of 340 MPa, more than an order of magnitude higher than the pristine MXene film with 29 MPa, originating from the attractive force between the two particles in water (which we analyzed with AFM) and further from the geometrical entanglement between them. (2) A high electronic conductivity of $2.95 \times 10^4 \text{ S m}^{-1}$, probably resulting from the small width of the CNF (around 3.5 nm) allowing better conductivity between the 2D flakes. (3) A high gravimetric capacitance of $\approx 298 \text{ F g}^{-1}$, since the addition of CNF does not limit the accessible sites for ion transport and pseudocapacitive charge storage. These combined metrics are higher than those previously reported for structural supercapacitor electrodes.^[1,5–7,11,29,30] We further showed that the MXene/CNF dispersion can be easily printed into various shapes for applications in electronics and micro-supercapacitors with high power and energy densities. Further fundamental studies on systems combining 1D and 2D materials should address questions about the effect of geometry and surface properties on the self-assembly process that defines

the properties of the nanocomposite. These systems can find more applications in areas such as structural energy storage,^[1] printed electronics and paper-based diagnostics.^[48]

Supporting Information

Supporting Information is available from the Wiley Online Library or from the author.

Acknowledgements

W.T. and A.V.M. contributed equally to this work. M.M.H. acknowledges the European Research Council (Grant No. 715268), W.T., Z.W., and M.H.H. acknowledge the Wallenberg Wood Science Centre at KTH for funding through the Knut and Alice Wallenberg Foundation. Z.W. acknowledges the Wenner-Gren Foundation for funding. A.V.M. acknowledges the support from Alabama EPSCoR Graduate Research Scholar Program (GRSP Round 12 and 13). M.B. acknowledges the support from Auburn University's Inramural Grants Program (IGP). The authors thank Innventia (RISE Sweden) for providing nanocellulose. W.T. and M.M.H. led the project and developed the idea. W.T. prepared and characterized the MXene/nanocellulose composites, conducted the electrochemical tests of microsupercapacitors, and analyzed the data with supervision by M.M.H. A.V.M. prepared and characterized MXene dispersions with supervision by M.B. A.V.M. conducted the electrochemical tests in three-electrode system, and analyzed the data. L.O. contributed to experiment design, designed the patterning on Whatman paper, prepared the micro-supercapacitor devices, and analyzed the data. M.R. prepared and characterized the CNC, and conducted the AFM force measurements. Z.W. and J.E. prepared the CNF dispersion, T.P. assisted for the AFM measurement and analyzed AFM data. L.W. contributed to the data analysis. M.M.H. supervised the research. All authors contributed to writing the manuscript.

Conflict of Interest

The authors declare no conflict of interest.

Keywords

2D titanium carbide, MXenes, nanocellulose, nanocomposites, supercapacitors

Received: May 9, 2019

Revised: June 20, 2019

Published online:

- [1] S. R. Kwon, J. Harris, T. Zhou, D. Loufakis, J. G. Boyd, J. L. Lutkenhaus, *ACS Nano* **2017**, *11*, 6682.
- [2] Y. Liu, K. He, G. Chen, W. R. Leow, X. Chen, *Chem. Rev.* **2017**, *117*, 12893.
- [3] N. Shirshova, H. Qian, M. Houllé, J. H. G. Steinke, A. R. J. Kucernak, Q. P. V. Fontana, E. S. Greenhalgh, A. Bismarck, M. S. P. Shaffer, *Faraday Discuss.* **2014**, *172*, 81.
- [4] W. Liu, M.-S. Song, B. Kong, Y. Cui, *Adv. Mater.* **2017**, *29*, 1603436.
- [5] J. Snyder, E. Gienger, E. Wetzel, *J. Compos. Mater.* **2015**, *49*, 1835.
- [6] D. O'Brien, D. Baechele, E. Wetzel, *J. Compos. Mater.* **2011**, *45*, 2797.
- [7] A. Sumboja, C. Y. Foo, X. Wang, P. S. Lee, *Adv. Mater.* **2013**, *25*, 2809.

- [8] D.-W. Wang, F. Li, J. Zhao, W. Ren, Z.-G. Chen, J. Tan, Z.-S. Wu, I. Gentle, G. Q. Lu, H.-M. Cheng, *ACS Nano* **2009**, *3*, 1745.
- [9] Z. Weng, Y. Su, D. W. Wang, F. Li, J. Du, H. M. Cheng, *Adv. Energy Mater.* **2011**, *1*, 917.
- [10] B. Anasori, M. R. Lukatskaya, Y. Gogotsi, *Nat. Rev. Mater.* **2017**, *2*, 16098.
- [11] Y. Xia, T. S. Mathis, M.-Q. Zhao, B. Anasori, A. Dang, Z. Zhou, H. Cho, Y. Gogotsi, S. Yang, *Nature* **2018**, *557*, 409.
- [12] M. R. Lukatskaya, O. Mashtalir, C. E. Ren, Y. Dall'Agnese, P. Rozier, P. L. Taberna, M. Naguib, P. Simon, M. W. Barsoum, Y. Gogotsi, *Science* **2013**, *341*, 1502.
- [13] M. R. Lukatskaya, S. Kota, Z. Lin, M.-Q. Zhao, S. Netanel, M. D. Levi, J. Halim, P.-L. Taberna, M. W. Barsoum, P. Simon, Y. Gogotsi, *Nat. Energy* **2017**, *2*, 17105.
- [14] M. Ghidui, M. R. Lukatskaya, M.-Q. Zhao, Y. Gogotsi, M. W. Barsoum, *Nature* **2014**, *516*, 78.
- [15] A. VahidMohammadi, M. Mojtavavi, N. M. Caffrey, M. Wanunu, M. Beidaghi, *Adv. Mater.* **2019**, *31*, 1806931.
- [16] M. Hu, C. Cui, C. Shi, Z.-S. Wu, J. Yang, R. Cheng, T. Guang, H. Wang, H. Lu, X. Wang, *ACS Nano* **2019**, *13*, 6899.
- [17] M. Naguib, V. N. Mochalin, M. W. Barsoum, Y. Gogotsi, *Adv. Mater.* **2014**, *26*, 992.
- [18] Z. Ling, C. E. Ren, M. Q. Zhao, J. Yang, J. M. Giammarco, J. Qiu, M. W. Barsoum, Y. Gogotsi, *Proc. Natl. Acad. Sci. USA* **2014**, *111*, 16676.
- [19] M. Boota, B. Anasori, C. Voigt, M. Q. Zhao, M. W. Barsoum, Y. Gogotsi, *Adv. Mater.* **2016**, *28*, 1517.
- [20] M. Zhu, Y. Huang, Q. Deng, J. Zhou, Z. Pei, Q. Xue, Y. Huang, Z. Wang, H. Li, Q. Huang, C. Zhi, *Adv. Energy Mater.* **2016**, *6*, 1600969.
- [21] A. VahidMohammadi, J. Moncada, H. Chen, E. Kayali, J. Orangi, C. A. Carrero, M. Beidaghi, *J. Mater. Chem. A* **2018**, *6*, 22123.
- [22] J. Yan, C. E. Ren, K. Maleski, C. B. Hatter, B. Anasori, P. Urbankowski, A. Sarycheva, Y. Gogotsi, *Adv. Funct. Mater.* **2017**, *27*, 1701264.
- [23] X. Xie, M.-Q. Zhao, B. Anasori, K. Maleski, C. E. Ren, J. Li, B. W. Byles, E. Pomerantseva, G. Wang, Y. Gogotsi, *Nano Energy* **2016**, *26*, 513.
- [24] Z. Wang, S. Qin, S. Seyedin, J. Zhang, J. Wang, A. Levitt, N. Li, C. Haines, R. Ovalle-Robles, W. Lei, Y. Gogotsi, R. H. Baughman, J. M. Razal, *Small* **2018**, *14*, 1802225.
- [25] M.-Q. Zhao, C. E. Ren, Z. Ling, M. R. Lukatskaya, C. Zhang, K. L. Van Aken, M. W. Barsoum, Y. Gogotsi, *Adv. Mater.* **2015**, *27*, 339.
- [26] A. S. Levitt, M. Alhabeb, C. B. Hatter, A. Sarycheva, G. Dion, Y. Gogotsi, *J. Mater. Chem. A* **2019**, *7*, 269.
- [27] M. Henriksson, L. A. Berglund, P. Isaksson, T. Lindström, T. Nishino, *Biomacromolecules* **2008**, *9*, 1579.
- [28] M. M. Hamed, A. Hajian, A. B. Fall, K. Hakansson, M. Salajkova, F. Lundell, L. Wågberg, L. A. Berglund, *ACS Nano* **2014**, *8*, 2467.
- [29] A. Hajian, S. B. Lindstrom, T. Pettersson, M. M. Hamed, L. Wågberg, *Nano Lett.* **2017**, *17*, 1439.
- [30] A. Malti, J. Edberg, H. Granberg, Z. U. Khan, J. W. Andreasen, X. Liu, D. Zhao, H. Zhang, Y. Yao, J. W. Brill, I. Engquist, M. Fahlman, L. Wågberg, X. Crispin, M. Berggren, *Adv. Sci.* **2016**, *3*, 1500305.
- [31] N. D. Luong, N. Pahimanolis, U. Hippi, J. T. Korhonen, J. Ruokolainen, L.-S. Johansson, J.-D. Nam, J. Seppälä, *J. Mater. Chem.* **2011**, *21*, 13991.
- [32] H. Lu, J. Hagberg, G. Lindbergh, A. Cornell, *Nano Energy* **2017**, *39*, 140.
- [33] J.-H. Kim, D. Lee, Y.-H. Lee, W. Chen, S.-Y. Lee, *Adv. Mater.* **2019**, *31*, 1804826.
- [34] W. Chen, H. Yu, S.-Y. Lee, T. Wei, J. Li, Z. Fan, *Chem. Soc. Rev.* **2018**, *47*, 2837.
- [35] D. Zhao, C. Chen, Q. Zhang, W. Chen, S. Liu, Q. Wang, Y. Liu, J. Li, H. Yu, *Adv. Energy Mater.* **2017**, *7*, 1700739.
- [36] L. Wågberg, G. Decher, M. Norgren, T. Lindström, M. Ankerfors, K. Axnäs, *Langmuir* **2008**, *24*, 784.
- [37] W.-T. Cao, F.-F. Chen, Y.-J. Zhu, Y.-G. Zhang, Y.-Y. Jiang, M.-G. Ma, F. Chen, *ACS Nano* **2018**, *12*, 4583.
- [38] T. Benselfelt, M. Nordenström, M. M. Hamed, L. Wågberg, *Nanoscale* **2019**, *11*, 3514.
- [39] M. D. Levi, M. R. Lukatskaya, S. Sigalov, M. Beidaghi, N. Shpigel, L. Daikhin, D. Aurbach, M. W. Barsoum, Y. Gogotsi, *Adv. Energy Mater.* **2015**, *5*, 1400815.
- [40] M. R. Lukatskaya, S. M. Bak, X. Yu, X. Q. Yang, M. W. Barsoum, Y. Gogotsi, *Adv. Energy Mater.* **2015**, *5*, 1500589.
- [41] S. Seyedin, E. R. S. Yanza, J. M. Razal, *J. Mater. Chem. A* **2017**, *5*, 24076.
- [42] J. Che, P. Chen, M. B. Chan-Park, *J. Mater. Chem. A* **2013**, *1*, 4057.
- [43] S. Dai, Y. Chu, D. Liu, F. Cao, X. Wu, J. Zhou, B. Zhou, Y. Chen, J. Huang, *Nat. Commun.* **2018**, *9*, 2737.
- [44] T. Li, S. X. Li, W. Kong, C. Chen, E. Hitz, C. Jia, J. Dai, X. Zhang, R. Briber, Z. Siwy, M. Reed, L. Hu, *Sci. Adv.* **2019**, *5*, eaau4238.
- [45] V. Augustyn, J. Come, M. A. Lowe, J. W. Kim, P.-L. Taberna, S. H. Tolbert, H. D. Abruña, P. Simon, B. Dunn, *Nat. Mater.* **2013**, *12*, 518.
- [46] J. Wang, J. Polleux, J. Lim, B. Dunn, *J. Phys. Chem. C* **2007**, *111*, 14925.
- [47] N. Kurra, B. Ahmed, Y. Gogotsi, H. N. Alshareef, *Adv. Energy Mater.* **2016**, *6*, 1601372.
- [48] M. M. Hamed, A. Ainla, F. Güder, D. C. Christodouleas, M. T. Fernández-Abedul, G. M. Whitesides, *Adv. Mater.* **2016**, *28*, 5054.